J Mater Sci (2024) 59:1215–1234

Ceramics

Enhanced visible light photocatalytic VOC oxidation via Ag-loaded TiO_2/SiO_2 materials

Carolina de Araújo Gusmão[1,*], Priscila Hasse Palharim[1], Bruno Ramos[1,2], Douglas Gouvea[3], Orlando Rodrigues Jr.[4], and Antonio Carlos Silva Costa Teixeira[1,*]

[1] *Research Group in Advanced Oxidation Processes (AdOx), Department of Chemical Engineering, Escola Politécnica, University of São Paulo, São Paulo, SP, Brazil*

[2] *Microfluidic and Photoelectrocatalytic Engineering Lab (μFEC), Department of Chemical Engineering, Centro Universitario FEI, São Bernardo do Campo, SP, Brazil*

[3] *Laboratory of Ceramic Processes (LPC), Department of Material Engineering, Escola Politécnica, University of São Paulo, São Paulo, SP, Brazil*

[4] *Nuclear and Energy Research Institute, IPEN/CNEN, São Paulo, SP, Brazil*

Received: 31 July 2023
Accepted: 14 December 2023
Published online: 16 January 2024

ABSTRACT

Ag-TiO_2/SiO_2 materials were synthesized with 1, 3, 5, and 10 wt% Ag contents and extensively characterized by different techniques, including XRD, SEM, TEM, XPS, BET, UV–VIS, EPR, and PL spectroscopy. Subsequently, the activity of these materials in the degradation of a model volatile organic compound (*n*-hexane) was compared by testing in a continuous gas–solid photoreactor. Loading with Ag induced stabilization of the brookite phase and crystal growth. TEM images showed d-spacing values corresponding to anatase and metallic silver. The specific surface area was lower in the Ag-modified catalysts, probably due to the blocking of the silica gel pores by Ag nanoparticles, whose size (~ 20 nm) was larger than the silica pores (~ 1.98 nm). SEM–EDS images showed heterogeneous distribution of Ag on the surface of the materials. XPS spectra showed bands referring to Ag^+ and Ag^0 3d, and Ti^{4+} and Ti^{3+} 2p. EPR analyses showed that silver loading of TiO_2/SiO_2 greatly increased the occurrence of oxygen vacancies in the material. Finally, the band gap energies calculated from the UV–VIS spectra were lower in the silver-containing catalysts, dropping from 3.25 to 3.17 eV in the optimal material. Under visible light, while TiO_2/SiO_2 showed no photoactivity, the Ag-modified materials presented satisfactory steady-state performance (46.4% *n*-hexane removal).

Handling Editor: David Cann.

Address correspondence to E-mail: carolina.argusmao@gmail.com; acscteix@usp.br

https://doi.org/10.1007/s10853-023-09285-7

GRAPHICAL ABSTRACT

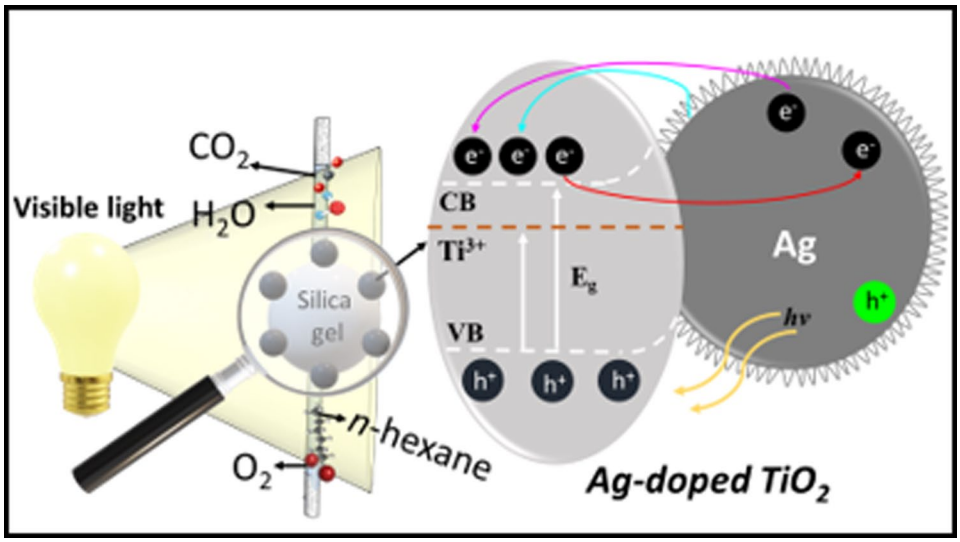

Introduction

The unbridled industrial expansion and exponential growth of the world population have led to a significant increase in toxic gas emissions, including compounds that can be highly harmful to human health [1]. For this reason, addressing the emissions of hazardous substances such as volatile organic compounds (VOCs) is a primary issue in the development of new and sustainable technologies [2–5].

VOCs are not only dangerous to human health but are also involved in reaction mechanisms that generate harmful by-products such as ozone and organic aerosols. Consequently, there are several research approaches spanning different technologies focused on removing these contaminants from industrial emissions. [6–8]. Strategies commonly applied for the removal of VOCs from air streams include modifications to existing equipment or process design, which are generally of limited efficiency, and the implementation of additional treatment technologies, which can be divided into *recovery* and *destructive* techniques. Recovery technologies, such as adsorption, are commonly used because of their high removal efficiency, but the difficulty associated to subsequent treatment leads to the investigation of less expensive technologies. In this context, catalytic oxidation emerges as an advantageous technique due to its potential for direct degradation of VOCs [3, 8]. Among the emerging technologies for the catalytic oxidation of volatile organic compounds, the use of *heterogeneous photocatalysis* has shown increasing success. Heterogeneous photocatalysis is an Advanced Oxidation Process (AOP) driven by photoactivated semiconductors that operate under mild temperature and pressure conditions [3–6, 8–11].

As environmental concerns grow, the emergence of photocatalysis as a sustainable and effective technology signals a promising path for the remediation of industrial emissions, offering several advantages such as eliminating the need for auxiliary chemicals in treatment processes, operating under ambient temperature and pressure conditions, and mineralizing hazardous organic contaminants into carbon dioxide, water, and harmless inorganic compounds [12]. Titanium dioxide (TiO_2), tungsten trioxide (WO_3) [13, 14], and zinc oxide (ZnO) [15, 16] stand out as remarkable semiconductors with significant potential as photocatalysts.

The most widely applied photocatalyst is titanium dioxide, which is attractive due to its low cost, high stability, simple preparation, and good efficiency in the degradation of different VOC contaminants [7, 9, 17, 18]. However, its large band gap energy and high charge carriers recombination rate may reduce the degradation efficiency and restrict its application under visible light [17, 19, 20]. To overcome this problem, modification of the semiconductors with metal particles, mainly noble metals, is an interesting alternative. Noble metal atoms can absorb light about $10^4 \sim 10^5$ times more than other metals and, consequently, can induce electric fields with 2 ~ 6 orders of

intensity higher than that of the incident light, which makes them suitable to be used for photocatalysis enhancement [21, 22]. Among different metals, silver is convenient due to its significant electrical and thermal conductivities, localized surface plasmon resonance properties, and relatively low cost [14, 20, 23–29]. Furthermore, doping with Ag leads to an increase in the concentration of oxygen vacancies located on the surface of the anatase grains. These oxygen vacancies give rise to unpaired electrons associated with Ti^{3+} species, thereby generating donor levels within the bandgap. This phenomenon can potentially enhance the separation of photogenerated charges and contribute to a reduction in the bandgap width [30–33].

The degradation of VOCs through gas-phase photocatalysis relies on a synergistic interaction between the catalyst, the irradiated light, and the organic contaminant [34]. As such, reactor configuration is a crucial factor in promoting improved performance and possible commercialization. In general, photocatalytic reactors are designed as flat plate [35], annular [36], wall-immobilized [37], packed bed [38], and fluidized bed reactors [39, 40]. Among these reactor types, *fluidized bed photocatalytic reactors* (FBPR) are particularly interesting for the treatment of VOC-containing gas streams, since they operate with low pressure drops and high throughputs, while providing highly efficient mass and heat transport properties, promoting good contact between reactants, allowing light transmission, and facilitating temperature control [41, 42]. However, since this type of reactor requires photocatalysts capable of fluidization, the use of bulk TiO_2 is not suitable because its cohesive forces surpass the gas drag forces [39]. Therefore, finding a suitable support structure to immobilize the catalyst is essential for the design of efficient treatment processes. In this regard, silica gel (SiO_2) emerges as an interesting candidate to support TiO_2 due to its large specific surface area and chemical stability, leading to better fluidization quality [42].

Most of the research on the photocatalytic degradation of VOCs in the gas phase focuses on unmodified TiO_2/SiO_2 materials under UV light [39, 40, 42, 43]. Lee et al. [44] and Lim and Kim [2] also studied photocatalysts loaded with metals (Cu and Pt) and metal oxides (CuO) applied in a fluidized bed reactor for the degradation of volatile organic compounds in the gas phase. However, both used ultraviolet light as the irradiation source and neither used silver in the catalyst formulation. In this way, a recent literature survey indicates that no studies have considered the photocatalytic activity of silver-modified TiO_2 supported on silica gel grains in a continuous gas-phase reactor under visible light. Furthermore, to the best of our knowledge, no previous studies have investigated the potential implications of Ag and Ag_2O loading for gas-phase photocatalytic reactions, specifically in terms of the generation of Ti^{3+} crystalline defects and oxygen vacancies. Therefore, this work aims to contribute to overcome the limitations of the application of heterogeneous photocatalysis in the degradation of VOCs under visible light, as well as to demonstrate how the modification of TiO_2 with silver also induces the formation of crucial crystal defects that enhance the photocatalytic properties of the materials. To this end, we synthesized fluidizable Ag-TiO_2/SiO_2 photocatalysts with different Ag contents and present an in-depth discussion of their morphological, optical, crystalline, structural, and paramagnetic properties. Subsequently, we compare their photocatalytic activity in a continuous gas–solid photoreactor for the conversion of a model VOC (*n*-hexane) under visible light, relating the discussed properties to the performance of the modified materials.

Materials and methods

Materials

Titanium IV isopropoxide (TTIP, 97%), silica gel 63–200 μm and $AgNO_3$ (> 99%) were purchased from Sigma-Aldrich. Nitric acid (HNO_3, 65%) and *n*-hexane (C_6H_{14}, 96%) were provided by Merck. These chemicals were used without any further purification. All solutions were prepared with pure water (18.2 MΩ cm) from a Milli-Q® Direct-Q system (Merck Millipore).

Photocatalysts synthesis

Coating of silica gel particles (specific surface area, 300 $m^2\ g^{-1}$) with TiO_2 nanocrystals was carried out using the acid sol–gel method described by Chen et al. [45], while Ag-loaded TiO_2/SiO_2 was synthesized using the same method adapted as follows: First, 8.4 mL of TTIP was added to 30 mL of 1-mol L^{-1} HNO_3 solution. Subsequently, 60 mL of Milli-Q® water was added to the solution, and the pH was increased to 1.5. After a stabilization period of 1 h, 20 mL of a 1.0 mol L^{-1} $AgNO_3$ solution was introduced. This corresponded to a final Ag content of 3% relative to the mass of TiO_2 in the

material. The resulting gel was irradiated by a UV-C lamp (OSRAM Puritec germicidal lamp HNS 8W G5 G8T5/OF) for 60 min under N_2 purge to promote silver photoreduction. Subsequently, the pH was increased to 2.0, and 2.2 g of silica gel was incorporated, making up a 60% TiO_2-40% silica gel mass ratio. Finally, the pH of the solution was adjusted to 3.0, and the gel was placed in dialysis membrane tubes immersed in a Milli-Q® water bath for 96 h. The gel obtained was then dried at 80 °C for 48 h and calcined at 450 °C for 240 min with a heating ramp of 5 °C min^{-1}. The same synthesis procedure was followed to synthesize catalysts containing 1, 5, and 10% silver relative to the mass of TiO_2 in the final material.

Ag-TiO_2/SiO_2 samples were prepared using four Ag contents for the synthesis approach. The synthesized samples were identified as X_Ag-TiO_2/SiO_2, in which X corresponds to the theoretical Ag content (%).

Characterization techniques

The particle size and morphology of the catalysts were investigated using scanning electron microscopy (SEM—FESEM JSM-7401F JEOL) coupled with energy-dispersive spectroscopy (EDS) (Thermo Scientific NSS spectral imaging). High-resolution transmission electron microscopy (HRTEM) images were acquired from a TEM JEOL JEM-2100 equipment. For this analysis, Ag-TiO_2/SiO_2 particles were dispersed in ethanol and immersed in an ultrasonic bath for 30 min. X-ray diffraction in the range $2\theta = 20–80°$ at a scan rate of 0.02° s^{-1} (D8 Focus—Bruker AXS, using Cu-K_α—0.154 nm) was applied to acquire information on the crystal structure, e.g., crystal phases, crystal size, lattice parameters, and microstrains. Diffuse reflectance spectroscopy (UV 2550, Shimadzu Co.) was used to evaluate the light absorption properties of the catalysts, while N_2 adsorption (Micrometrics Gemini III 2375) was applied to estimate their specific surface area using the Brunauer–Emmett–Teller (BET) method. The effective Ag content in the Ag-TiO_2/SiO_2 materials was estimated by X-ray-dispersive energy (EDX) fluorescence spectroscopy (NEX-RIGAKU). X-ray photoelectron spectroscopy (Thermo Scientific, K-Alpha, Al Kα 1486.6 eV, X-ray spot size of 400 µm, 10^{-8} mBar) was used to assess the energy states of the elements on the photocatalytic surface. For this analysis, 5 mg of the TiO_2/SiO_2 catalysts was adhered to an aluminum strip and degassed in an ultra-high vacuum (UHV) chamber at 25 °C. The segregation of Ag on the surface was investigated by analyzing the composition of the leaching water by means of optical emission spectroscopy with inductively coupled plasma (ICP) using an iCAP 6300 Duo (Thermo Scientific), after thoroughly washing the samples in an acidic medium. The pure TiO_2/SiO_2 and 3_Ag_TiO_2/SiO_2 materials were analyzed by electron paramagnetic resonance (EPR) spectroscopy (Bruker—EMX Plus). Finally, photoluminescence spectra were acquired at room temperature by a Fluorolog-3-fluorospectrophotometer equipped with a Xe lamp as excitation irradiation.

Experimental unit

The photocatalytic activity tests were carried out in a gas–solid reactor (GSPR), which consists of a borosilicate glass tube with a length of 120 mm and an internal diameter of 10 mm. The ends of the tube were packed with glass wool to retain the photocatalytic bed. The irradiated part of the fluidized bed reactor was completely loaded by solids in all experiments, resulting in a bed height of 7 cm or an irradiated volume of 1.5 mL. The reactor is housed in an experimental unit designed for photocatalytic testing as shown in Fig. 1a.

The experimental setup consists of a stream of pure oxygen supplied by a gas bottle, which is divided into three separate streams. The first stream passes through a water bubbler to regulate its humidity. The second stream consists of pure oxygen. The third stream passes through an *n*-hexane diffusion tube with an inner diameter of 5 mm and a height of 300 mm, immersed in a thermostatic bath set at 5 °C. The purpose of this stream is to control the *n*-hexane inlet concentration by adjusting the temperature of the thermostatic bath. The flow rates of the three O_2 streams are controlled by three mass flow meters (D6FP0001A1, Omron), which operate in the range of 0–100 mL min^{-1}. The humidity of the gas stream was measured by an ITHT2210 hygrometer (Instrutemp), adjacent to the inlet of the glass reactor. The temperature of the inlet stream was maintained in a range of 20–25 °C.

The reactor was irradiated by a visible light irradiation source in order to evaluate the photocatalytic activity of the different materials under visible light. The irradiation source was a 50-W LED chip provided by LG with wavelength emission centered at around 405 nm. The LED chip was positioned 36.0 cm away from the reactor to ensure homogeneous irradiation throughout its volume by the light source. The

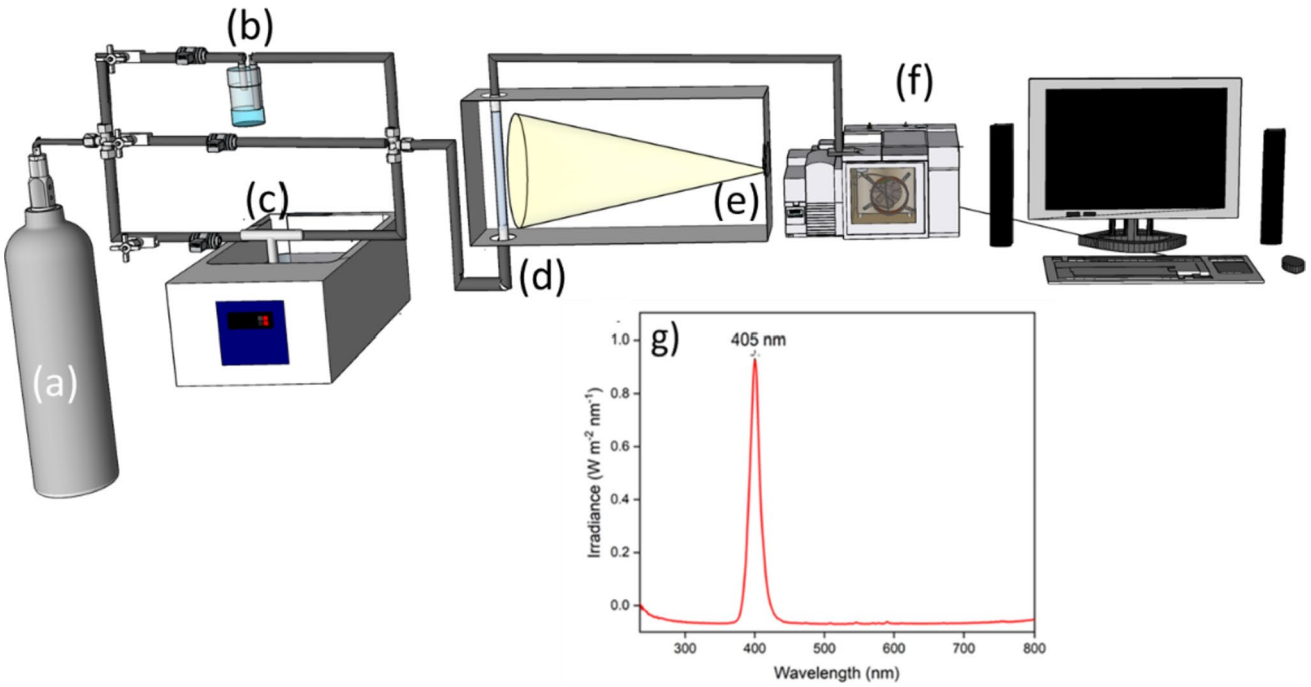

Figure 1 **a** Description of the experimental unit: **a** oxygen bottle; **b** humidifier; **c** *n*-hexane diffusion tube; **d** gas–solid photocatalytic reactor; **e** light source; **f** GC-PID/TiD gas chromatograph; **g** irradiance spectrum on the reactor surface provided by a 50-W LED chip.

irradiance spectra delivered by the LED@450 nm on the reactor surface were measured with a spectroradiometer (SPR-4002, Luzchem Research, Inc.) and are shown in Fig. 1g.

The experiments were performed by setting the operating conditions, i.e., humidity, radiant flux, and *n*-hexane inlet concentration, to 50%, 1.1 mW cm^{-2}, and 80 ppm, respectively, and the catalyst sample inside the reactor was varied to evaluate the influence of Ag content in Ag-TiO_2/SiO_2 materials on the reactor performance under visible light. The light source was switched on when adsorption equilibrium was reached, i.e., when the *n*-hexane concentration at the reactor outlet was equal to that at the inlet. This condition was checked using a bypass line that directly connected the reactor inlet to the gas chromatograph. The *n*-hexane concentration at the reactor outlet was monitored continuously by an in-line GC-PID/TiD gas chromatograph. The GC-PID/TiD analyzed a 98-µL sample of air injected from its loop on a Restek RTX-Volatiles column (30 m, 0.32 mm i.d., 2.0 µm thick) with N_2 as carrier gas and an oven temperature of 70 °C without heating ramp. The *n*-hexane content in the gas stream was quantified using a photoionization detector equipped with a Krypton gas lamp (10.6 eV) at an operating temperature of 200 °C. The performance of the different photocatalysts was evaluated with respect to the steady-state *n*-hexane conversion, *X* (Eq. 1), and the apparent reaction rate, *R* (Eq. 2). In these equations, C_i and C_0 denote the steady-state concentrations at the inlet and outlet of the reactor, respectively; *Q* is the gas flow rate through the reactor; and *m* is the mass of TiO_2.

$$X = \frac{C_i - C_0}{C_i} \tag{1}$$

$$R = \frac{Q \times (C_i - C_0)}{m} \tag{2}$$

Results and discussion

Catalysts characterization

Crystalline properties

Table 1 summarizes all samples synthesized in this investigation. Figure 2 shows the diffractograms of the catalysts with different Ag contents, identified as previously explained in Sect. "Photocatalysts

Table 1 Crystallite size, lattice parameters, and weight fraction of the crystalline phases, obtained from Rietveld refinement by XRD analysis

Sample	Crystallite size (nm)			Lattice parameters (Å)							Weight fraction (%)		
	Anatase	Rutile	Brookite	Anatase		Rutile		Brookite			Anatase	Rutile	Brookite
				a, b	c	a, b	c	a	b	c			
TiO_2/SiO_2	4.76			3.76	9.42	–	–	–	–	–	100%	–	–
1_Ag-TiO_2/SiO_2	5.99	–	3.57	3.77	9.45	–	–	5.17	9.19	5.46	99.6	–	0.4
3_Ag-TiO_2/SiO_2	6.25	–	3.62	3.76	9.46	–	–	5.11	9.49	5.66	95.3	–	4.7
5_Ag-TiO_2/SiO_2	5.99	–	6.23	3.77	9.44	–	–	5.15	9.19	5.46	99.6	–	0.40
10_Ag-TiO_2/SiO_2	4.48	–	2.79	3.76	9.42	–	–	5.15	9.19	5.46	98.3	–	1.70

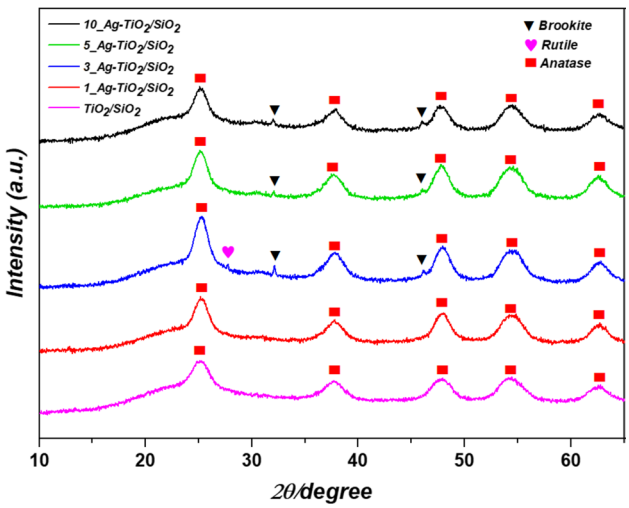

Figure 2 XRD patterns of TiO_2/SiO_2 and 1, 3, 5, and 10_Ag-TiO_2/SiO_2.

synthesis." All materials show peaks referring to the anatase crystalline phase, with the most intense peaks at $2\theta = 25.3$, 37.5, 48, 55, and 63°, corresponding to the crystalline planes (011), (004), (020), (015), and (024), respectively, according to JCPDS card no. 96–720-6076.

The intensity ratio between the (011) and (004) planes remained relatively consistent at around 2 for all the materials, except for 3_Ag_TiO_2/SiO_2, which was measured equal to 2.42 due to the notably higher intensity of the (011) plane. A similar trend was noted in the comparison of peaks corresponding to the (001) plane with those from (020), (015), and (024) for the materials. The ratio of intensity between two different crystallographic planes in anatase can be altered by various factors, including the presence of crystal defects, such as oxygen vacancies, which can serve as nucleation sites for specific crystallographic planes, affecting their exposure [46, 47].

In addition, samples 3, 5, and 10_Ag_TiO_2/SiO_2 showed typical peaks of the brookite phase at $2\theta = 32.11$ and 46.25°, corresponding to planes (121) and (230), according to JCPDS card no. 96–900-4139. Although anatase is usually the dominant phase formed during sol–gel synthesis of TiO_2, when precipitation is carried out in acidic medium at low temperatures, brookite can be formed as a by-product [48]. This fact can be attributed to preferential deoxolation over olation in acidic medium. As a result, the subsequent condensation of the molecules is oriented along the apical direction, thereby promoting the formation of both anatase and brookite chains [49]. Due to the minimal brookite content in the materials, as indicated by XRD (maximum of 1.71%, estimated by Rietveld refinement), its presence is assumed to have no discernible impact on photocatalytic activity. This implies that any potential effects of brookite are overshadowed by other factors, which will be discussed further below.

Moreover, regarding the XRD results, only the diffractogram concerning sample 3_Ag_TiO_2/SiO_2 showed a rutile peak at $2\theta = 27.6°$, corresponding to the crystallographic plane (110). Previous studies have indicated that the presence of silica as a support material can hinder the transformation from anatase to rutile [50]. However, the incorporation of Ag ions induced the formation of oxygen vacancies in the anatase grains for 3_Ag_TiO_2/SiO_2, as will be discussed later in the section on optical properties. As the anatase to rutile phase conversion entails the movement of titanium and oxygen ions, the formation of oxygen vacancies allows space for the reorganization of ions during phase transition and lowers the energy

required for structural reordering. Concurrently, the defects decrease the number of broken Ti–O bonds and reduces energy consumption, facilitating the phase conversion. It is worth noting that the generation of oxygen vacancies for the 3_Ag_TiO_2/SiO_2 material was much more intense than for the others, as will be subsequently presented in the optical properties section, which explains why only this material exhibited the rutile phase in its diffractogram [33, 51, 52].

The explanation for this phenomenon lies in the size disparity between Ag^+ ions (approximately 126 pm) and Ti^{4+} ions (approximately 68 pm). As a result, the Ag^+ ions introduced during the sol–gel process cannot effectively integrate into the lattice of the anatase phase to establish a solid solution. During the subsequent drying stage at 70 °C and the calcination process at 450 °C, Ag^+ ions gradually migrate toward the surface of TiO_2. Importantly, the calcination process involves high temperatures, which, combined with the reducing nature of titanium dioxide, facilitate the reduction of Ag^+ ions on the surface, causing a partial transformation into metallic Ag. The reduction of Ag^+ ions plays a role in the charge balancing, leading to the generation of oxygen vacancies on the surface of TiO_2, which further promotes the formation of the rutile phase [51, 52].

Furthermore, due to the weaker bonding strength of Ag–O compared to Ti–O and Ag–Ag bonds and the higher surface free energy of Ag atoms compared to TiO_2 [33], the calcination process promotes aggregation of Ag atoms into metallic Ag particles and clusters. The sizes of these aggregates typically range between 2 and 10 nm. It should be noted that no diffraction peaks corresponding to metallic silver were observed in the XRD analysis. This absence could be attributed to the low actual silver content present in the samples, as indicated in Table 2.

The crystallite sizes, lattice parameters, and weight fraction of the crystalline phases of TiO_2 were determined using Rietveld refinement, as shown in Table 1.

Regarding crystallite sizes, no significant variation was observed for the different samples, with all silver-loaded samples showing subtly larger crystallite sizes than those of TiO_2/SiO_2. During the calcination phase, Ag^+ ions migrate to the TiO_2 surface, hindering diffusion, and rearranging the Ti^{4+} and O^{2-} ions required for grain growth. However, the slight increase in crystal size observed can be attributed to the early formation of metallic Ag and agglomerates during the calcination process, which is accompanied by an increase in Ag + density on the anatase surface. In this scenario, the inhibitory effect on crystal growth typically associated with Ag loading is effectively suppressed [33]. The slight variation in the lattice parameters observed for the different materials, as shown in Table 1, indicates that there is no metal substitution occurring in the crystal lattice. This observation is supported by the difference in ionic radius between Ti^{4+} (74.5 pm) and Ag^+ (129 pm). The substantial difference in ionic radii would lead to a significant distortion of the crystal lattice and consequently result in a noticeable variation of the lattice parameters. According to the Hume-Rothery rule [53], ionic substitution occurs only when the difference between the ionic radii of the substituents is less than 15%. In this case, the radius of Ag^+ is approximately 73% larger, which further supports the hypothesis that silver cannot substitute for Ti in the crystal lattice.

Table 2 S_{BET}, Ag weight fraction, band gap energy, and band potential energies of all synthesized photocatalyst samples

Sample	Theoretical Ag content (% wt/wt TiO_2)	Effective Ag content (% wt/wt TiO_2)	Specific surface area ($m^2\ g^{-1}$)	E_g[1] (eV)	E_{CB}[2] (eV)	E_{VB}[3] (eV)
TiO_2/SiO_2	0	0	294.6	3.20	−0.26	2.94
1_Ag-TiO_2/SiO_2	1	0.11	259.9	3.08	−0.20	2.88
3_Ag-TiO_2/SiO_2	3	0.27	243.3	3.07	−0.20	2.87
5_Ag-TiO_2/SiO_2	5	0.31	238.9	3.09	−0.20	2.89
10_Ag-TiO_2/SiO_2	10	0.79	167.6	3.16	−0.20	2.96

[1] E_g band gap energy,

[2] E_{CB} conduction band potential,

[3] E_{VB} valence band potential

Morphology and surface properties

Table 2 shows that the effective silver content in the synthesized materials, as evaluated by EDX analyses, was much lower than the nominal silver content used in the synthesis procedure. Apparently, silver was retained in the dialysis membrane used in the synthesis, which was initially transparent and visually darkened after the washing step. As the membrane allows ions to pass through, it is assumed that ionic silver was retained on its surface, as it was converted to metallic silver in ambient light. Therefore, to simplify the discussion of the materials, they are named X_Ag-TiO_2/SiO_2 according to their theoretical X content, but all discussions were conducted considering the effective silver content in the samples.

Figure 3 shows SEM images of TiO_2/SiO_2, 3_Ag_TiO_2/SiO_2 and 10_Ag_TiO_2/SiO_2. In all of them, the particles exhibit heterogeneous morphology, substantial variability in mean diameter size, as well as irregular shapes and rough surfaces. SEM images show that increasing Ag content favors TiO_2 agglomeration as well as a decrease in particle size. The elemental EDS spectra (Fig. 3g) at the points highlighted in red in Fig. 3d and f indicate the presence of clusters of Ag NPs on the TiO_2 surface. The EDS

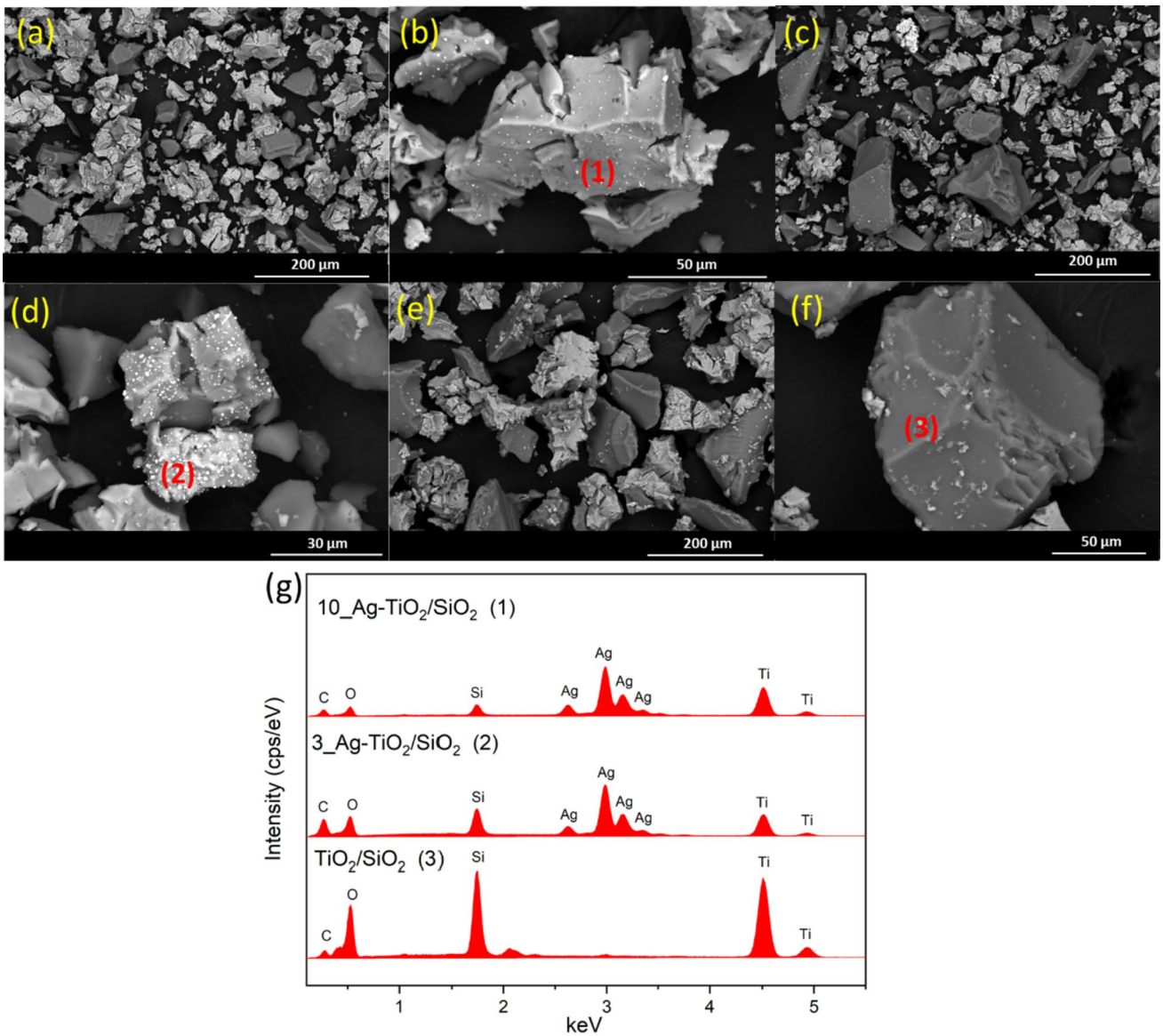

Figure 3 SEM and elemental EDS spectra of the samples: **a**, **b** TiO_2/SiO_2; **c**, **d** 3_Ag-TiO_2/SiO_2; **e**, **f** 10_Ag-TiO_2/SiO_2; **g** EDS spectra.

spectra also show a low intensity of the silica peak in sample 10_Ag-TiO_2/SiO_2, which may suggest the existence of unsupported TiO_2 grains.

Transmission electron microscopy (TEM) analysis was performed for the 3_Ag-TiO_2/SiO_2 and 10_Ag-TiO_2/SiO_2 samples to obtain more information about the size and distribution of TiO_2 crystals and silver nanoparticles (Fig. 4). Figure 4a, b, and c shows the TEM and HRTEM images for 3_Ag-TiO_2/SiO_2. It is possible to see a TiO_2 cluster supporting Ag nanoparticles of around 20 nm in size with a uniform, spherical geometry. Noble metal nanoparticles larger than 2 nm are considered to be large positive nuclei surrounded by a cloud of free electrons, allowing *localized surface plasmonic resonance* (LSPR) to occur [22], a mechanism that contributes to increased photocatalytic activity. This resonance can result in a strong increase in the local electromagnetic field, which acts as an energy transfer center through a process known as plasmonic resonance energy transfer (PRET) [54]. When transferred to TiO_2, this energy can be used to create more electron–hole pairs. This phenomenon is typically observed in NPs smaller than 30 nm, such as those found in 3_Ag_TiO_2/SiO_2 [55].

Figure 4b and c shows HRTEM images of the same material, exhibiting a d-spacing of 3.50 Å that corresponds to the crystallographic plane (101) of anatase, according to JCPDS card no. 21–1272. A d-spacing of 2.3 Å is also observed in the image, corresponding to the crystallographic plane (111) of metallic silver, according to JCPDS card no. 04–0783. These analyses corroborate the findings discussed earlier that Ag^+ during calcination migrated to the surface of the anatase grains, being reduced to Ag^0, which forms aggregates due to the high surface energy of Ag. The d-spacing (3.50 Å) corresponding to anatase is slightly lower than the standard value (3.51 Å), another indication that there is no substitution of Ti^{4+} by Ag^+, since such a substitution should introduce a compressive transverse microstrain in the crystal lattice [56], which would lead to higher d-spacing values than the standard. The TEM and HRTEM images of the 10_Ag-TiO_2/SiO_2 sample shown in Fig. 4d, e, and f suggest that the Ag nanoparticles were mostly segregated and formed several clusters in the material. The comparison of

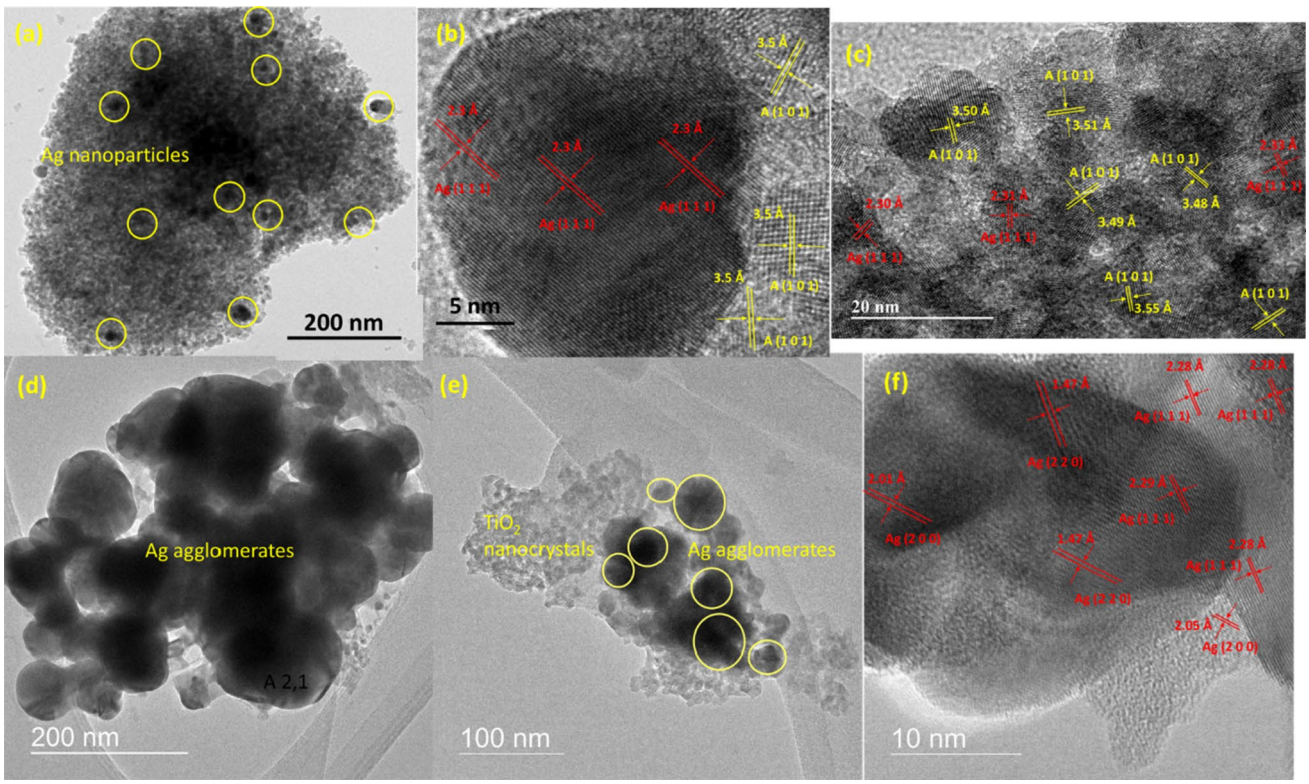

Figure 4 **a** TEM image of 3_Ag-TiO_2/SiO_2; **b**, **c** HRTEM image of 3_Ag-TiO_2/SiO_2; **d**, **e** TEM image of 10_Ag-TiO_2/SiO_2; **f** HRTEM image of 10_Ag-TiO_2/SiO_2.

Fig. 4a and d highlights the contrast in the distribution of Ag NPs in TiO_2; while the 3_Ag-TiO_2/SiO_2 sample presented Ag NPs distributed on the TiO_2 surface, large clusters of metallic silver can be observed in 10_Ag-TiO_2/SiO_2, and most are not anchored to the TiO_2 particles. The HRTEM image of 10_Ag-TiO_2/SiO_2 (Fig. 4f) exhibited d-spacing values corresponding to different crystallographic planes of metallic silver, especially (111), (200), and (220). In contrast, no d-spacing corresponding to crystallographic planes of anatase was identified.

It is worth noting that the HRTEM images did not reveal any characteristic d-spacing of the brookite phase identified in XRD patterns. This discrepancy can be attributed to the relatively low content of this phase in the sample, as indicated by the low intensity of the corresponding diffraction peaks.

Figure 5 schematically illustrates the distribution of TiO_2 crystals and silver nanoparticles revealed by SEM and TEM results. It can be seen that TiO_2 is dispersed on the silica gel support. The same material synthesized with an intermediate silver content (3_Ag-TiO_2/SiO_2) presented single Ag NPs anchored to TiO_2. For the highest silver content (10_Ag-TiO_2/SiO_2), Ag NPs were dispersed on the TiO_2 surface, but also forming agglomerates, being segregated from titanium dioxide. As discussed earlier, the high surface free energy of silver promotes the aggregation of this phase rather than its anchoring to TiO_2. This phenomenon is even more pronounced in sample 10_Ag-TiO_2/SiO_2, given its higher silver concentration.

The S_{BET} analysis results of the synthesized materials are also summarized in Table 2. The S_{BET} reduced as the Ag content increased, due to the larger number of SiO_2 pores blocked by Ag nanoparticles and Ag clusters [57]. It is suggested that Ag NPs are arranged not only on the TiO_2 surface but also on the support (SiO_2). Thus, due to their average size (~ 20 nm) observed in TEM images, Ag NPs could not fill the silica pores [34], depositing on the surface and, consequently, blocking the pores [58–60].

XPS analyses were carried out on the TiO_2/SiO_2 material and the 3_Ag_TiO_2/SiO_2 sample to assess the impact of the presence of silver on the generation of Ti^{3+} (Fig. 6a and b). The spectra obtained revealed a remarkable rightward shift in the peaks corresponding to Ti 2p3/2 and Ti 2p1/2 in the loaded sample (Fig. 6b) compared to the unloaded one (Fig. 6a). By deconvoluting the peaks, it was determined that the TiO_2/SiO_2 sample had 90% Ti^{4+} and 10% Ti^{3+}, whereas the Ag_TiO_2/SiO_2 sample showed 15% Ti^{4+} and 85% Ti^{3+}. It is suggested that Ti^{3+} was formed to counterbalance the oxygen vacancies in the crystal lattice resulting from the photoreduction of Ag on the surface of the anatase grains, as mentioned above. The Ti^{3+} and the oxygen vacancies can improve the photocatalytic activity of the material by increasing its electron conductivity and light absorption [61].

Figure 6c and d presents the high-resolution XPS spectra of the O 1 s electronic state of the TiO_2/SiO_2 (Fig. 6c) and 3_Ag-TiO_2/SiO_2 (Fig. 6d) materials. The bands appearing at 532.8, 532.1, and 529.6 eV correspond to adsorbed water, Si–O, and Ti–O, respectively, for TiO_2/SiO_2 (Fig. 6c). As for the 3_Ag-TiO_2/SiO_2 material, the bands appearing at 533.1, 531.8, 529.6, and 528.4 eV correspond to adsorbed water, Si–O, Ti–O, and Ag–O bonds, respectively.

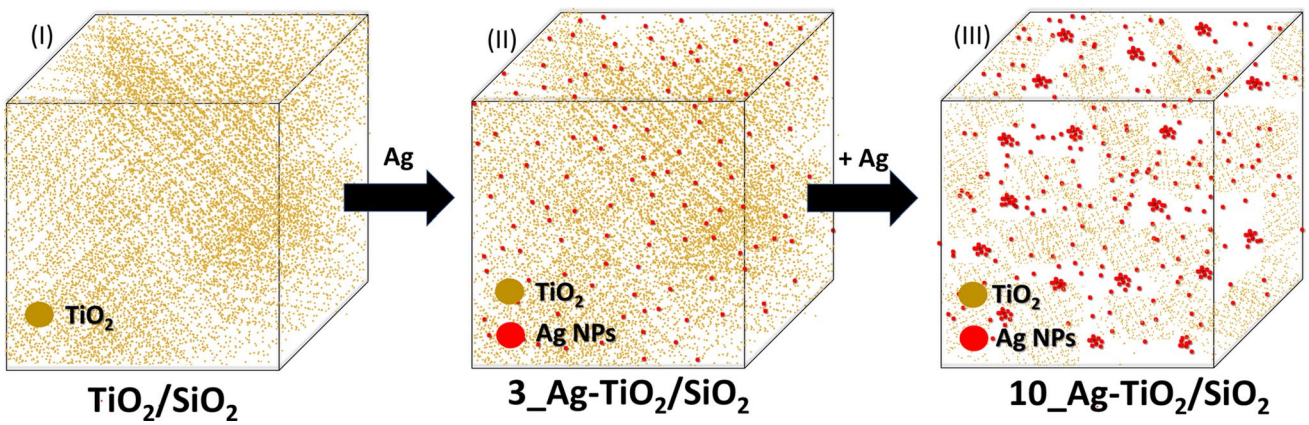

Figure 5 Schematic illustration of the distribution of Ag NPs on TiO_2 for 3_Ag-TiO_2/SiO_2 (II) and 10_Ag-TiO_2/SiO_2 (III).

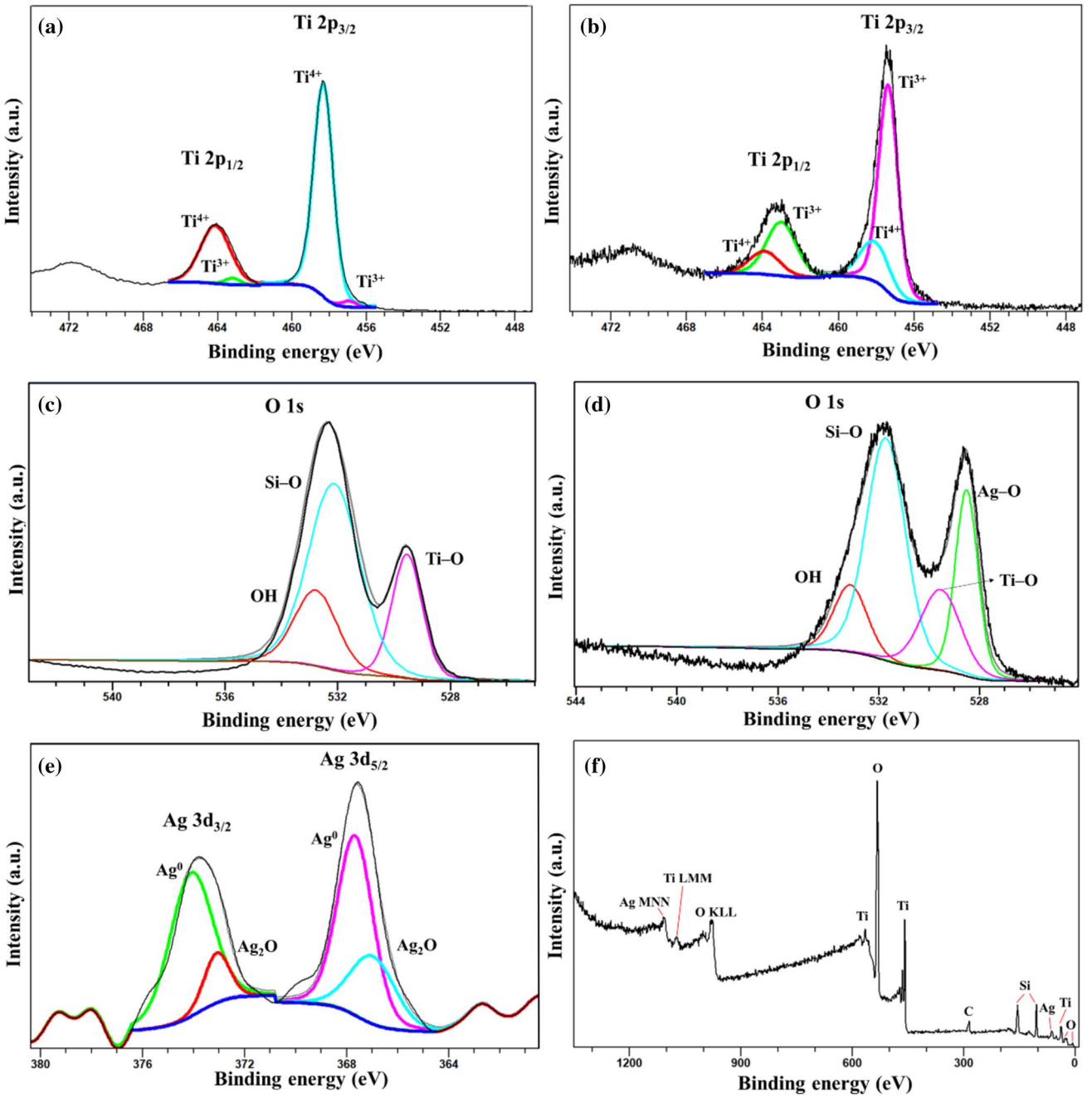

Figure 6 XPS high-resolution spectra of: **a** Ti 2p for the TiO_2/SiO_2 sample; **b** Ti 2p for the 3_Ag-TiO_2/SiO_2 sample; **c** O 1 s for the TiO_2/SiO_2 sample; **d** O 1 s for the 3_Ag-TiO_2/SiO_2 sample; **e** Ag 3d of the 3_Ag-TiO_2/SiO_2 sample; **f** survey spectrum of 3_Ag-TiO_2/SiO_2.

Figure 6e shows the deconvolution for sample 3_Ag_TiO_2/SiO_2 of high-resolution Ag 3d XPS spectra into bands corresponding to Ag (368.1 and 374.3 eV) and Ag_2O (367.6 and 373.6 eV), consisting of 72% of Ag and 28% of Ag_2O [62]. The state Ag^+ suggests that, during calcination, silver was partially reduced to Ag^0, with part of it remaining as Ag_2O on the surface [33].

The survey spectrum of 3_Ag-TiO_2/SiO_2 shown in Fig. 6f was used to determine the elemental composition of the surface of the Ag-loaded material. This analysis aimed to compare the weight fraction of Ag^+

and Ag^0 on the surface by means of XPS analysis and the bulk composition by means of EDX analysis. For this, an empirical approach based on the estimated areas of the main species bands was used, according to Eq. 8, where x_i is the molar fraction of element i, A_i is the area of each main band, s_i is the relative sensitivity factor (RSF) [53], and n is the number of elements ($n = 4$ for this case).

$$x_i = \frac{A_i/s_i}{\sum_{j=1}^{n}(A_j/s_j)} \tag{8}$$

The mole fractions were converted into mass concentrations, and Table 3 shows that results are in good agreement with those obtained by EDX analysis for the same material. It is observed that the molar percentage of silver obtained from XPS is higher, which suggests segregation of Ag^0 and Ag^+ on the catalyst surface. It is worth noting that due to its working principle, the XPS analysis is more appropriate to quantify the atomic concentrations of the elements on the surface of materials, whereas the EDX is a standard technology for assessing the overall composition of the sample. The XPS is also considered a sensitive analytical technique due to the consideration of the attenuation of X-ray intensities as a function of the electron escape depth [63]. To enhance the robustness of the findings when comparing the quantification of elements using XPS for surface analysis and EDX for bulk analysis, we conducted a rigorous washing procedure on the 3_Ag_TiO_2/SiO_2 material. This involved three cycles of centrifugation with a 1-M HCl solution. Subsequently, the resulting supernatant underwent ICP analysis to ascertain the quantity of silver present on the surface. As illustrated in Table 3, the reduction in the mass content of silver after washing strongly suggests that practically all the silver content has been segregated on the surface of the catalyst. This observation aligns with the results from the quantitative XPS and EDX analyses.

Table 3 Weight percentage of TiO_2, SiO_2, and Ag in 3_Ag-TiO_2/SiO_2 material by EDX, XPS, and ICP element analysis

Composite	Weight percentage (%)		Loss percentage (%)
	EDX	XPS	ICP
TiO_2	58.2	55.31	–
SiO_2	41.4	46.49	–
Ag	0.162	0.183	0.126

Optical properties

The band gap energy (E_g) was calculated for each photocatalytic material using the Kubelka–Munk function [34, 64, 65] (Eqs. 5 and 6), in which R is the diffuse reflectance (%) obtained by UV–VIS analyses, $h\upsilon$ is the photon energy (eV) corresponding to the wavelength λ, as $h\upsilon = 1240/\lambda$, and n is the factor related to the type of electronic transition: as TiO_2 is an indirect semiconductor, $n = 2$ [66]. The band gap energy is calculated from the intersection point of a tangent line along the inflection point of the curve with the horizontal axis (Fig. S1). Increasing silver content in the photocatalyst gradually reduced its band gap energy.

$$F(R) = \frac{(1-R)^2}{2 \times R} \tag{5}$$

$$(F(R) \times h\upsilon)^{\frac{1}{n}} = A(h\upsilon - E_g) \tag{6}$$

As the band gap energy is a key parameter in photocatalytic activity, it is worth discussing which mechanisms triggered by Ag NPs affect the band gap modifications of TiO_2/SiO_2. The Schottky barrier, which will be further discussed in this paper, has no effect on the band gap energy, increasing the photocatalytic activity only by decreasing charge recombination [55]. The presence of Ti^{3+} crystalline defects acts as an effective method of increasing visible light absorption by creating additional mid-bandgap states, which are observed below the conduction band [31]. These mid-bandgap states, resulting from Ti^{3+} and oxygen vacancies, act as electronic donor states, further contributing to the overall enhancement of visible light absorption [30, 31, 67, 68].

As the XPS analysis evidenced the presence of Ti^{3+} defects on the photocatalytic surface of the silver-modified material, further investigation of the oxygen vacancies in the materials was carried out by means of electron paramagnetic resonance (EPR) spectroscopy. Figure 7a compares the EPR spectra of pure TiO_2, TiO_2/SiO_2, 3_Ag_TiO_2/SiO_2, and 10_Ag_TiO_2/SiO_2. It is clear that a substantial increase in the g-factor signal of 1.998, corresponding to oxygen vacancies, occurs when titanium dioxide

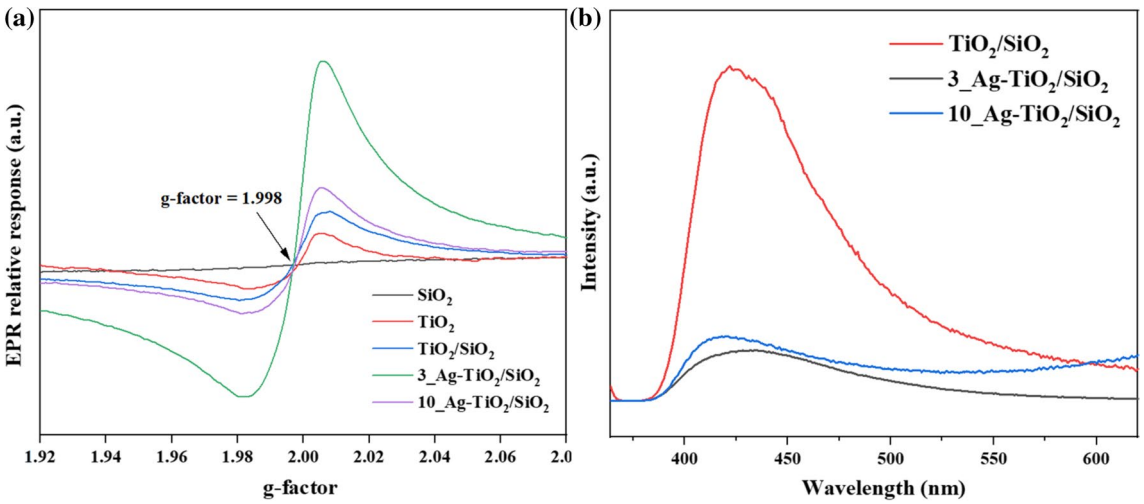

Figure 7 **a** EPR spectra of SiO_2, TiO_2, TiO_2/SiO_2, 3_Ag-TiO_2/SiO_2, and 10_ Ag-TiO_2/SiO_2; **b** PL spectra of TiO_2/SiO_2, 3_Ag-TiO_2/SiO_2, and 10_Ag-TiO_2/SiO_2.

is associated with silica gel [69]. In Ag-loaded samples, this may also result from the partial photoreduction of Ag_2O to metallic silver on the surface of anatase grains, which induce the effusion of lattice oxygen and, consequently, the formation of oxygen vacancies. It is worth noting that this increase in the density of oxygen vacancies, when comparing the EPR spectra of the TiO_2/SiO_2 and 3_Ag_TiO_2/SiO_2 materials, aligns with the results of the XPS analysis, which showed an increase in the concentration of Ti^{3+}. However, when the silver content was increased (10_Ag_TiO_2/SiO_2), a reduction in the EPR signal was observed. This behavior is likely due to the formation of larger metallic Ag clusters far from the surface of the anatase grains, which may prevent the formation of permanent crystalline defects in the semiconductor structure.

Finally, photoluminescence (PL) emission spectra were obtained to investigate the separation and recombination behavior of photogenerated charge carriers. The emission spectra were obtained for the different samples excited at 314 nm at room temperature, as shown in Fig. 7b. The catalyst containing the optimum Ag content showed much lower band intensity compared to unloaded TiO_2/SiO_2. It is known that the intensity of the photoluminescence emission spectra of TiO_2 is greatly dependent on the recombination of the photogenerated charges [70–73]. The result suggests that the Schottky barrier, which will be discussed later, reduced the charge recombination rate in Ag-modified photocatalysts [55], sharply decreasing the intensity of the typical band of TiO_2 at 420 nm [74, 75]. On the other hand, the catalyst containing a silver content above "optimal" showed a slightly higher intensity band at 420 nm and a larger increase above 550 nm, which is characteristic of a higher recombination of electrons in trap energy states (Ag NPs) and positive holes [76]. This is likely due to the reduction of crystal defects density on the semiconductor surface, as already mentioned, which acted as charge recombination suppressors [30, 32]. The presence of crystalline defects, specifically Ti^{3+} oxidation states and oxygen vacancies, as verified through rigorous EPR and XPS analyses, exerts a direct influence on minimizing charge recombination. These defects have the ability to capture charge carriers, thereby modulating the overall performance of the material [30].

Photocatalytic performance

The performance of each composite material was evaluated by comparing its reactivity toward the oxidation of *n*-hexane in a contaminated gas stream. Control experiments were performed to evaluate the effect of irradiation on *n*-hexane concentration as well as the effect of the material without irradiation; in neither case was a measurable difference observed between the inlet and outlet concentrations of the contaminant. After the light source was turned on, steady-state conversions were determined when the contaminant concentration stabilized in ten consecutive samples.

Table 4 Evaluation of the photocatalytic activity of TiO_2/SiO_2 materials with different Ag contents

Material	*n*-hexane degradation (%)	Reaction rate ($\mu mol.gTiO_2^{-1}.h^{-1}$)
TiO_2/SiO_2	6.2	0.60
1_Ag-TiO_2/SiO_2	17.4	1.83
3_Ag-TiO_2/SiO_2	46.4	4.33
5_Ag-TiO_2/SiO_2	9.2	0.98
10_Ag-TiO_2/SiO_2	0.2	0.013

Table 4 compares the reaction rates and *n*-hexane conversions obtained for catalysts with different silver contents under visible light, for a space–time of 4.7 s. Figure 8a shows the evolution of the *n*-hexane concentration at the reactor outlet over time before and after switching on the visible LED for the 3_Ag_TiO_2/SiO_2 material, while Fig. 8b compares the photocatalytic performance of the materials. Since this is a continuous gas-phase reactor, after switching on the lamp, a transient regime is observed until the system has not yet reached steady-state conditions. When comparing the materials, the presence of Ag nanoparticles significantly improved the catalyst photoactivity, increasing the degradation of *n-hexane* from 6.0% to 46.2% for 3_Ag_TiO_2/SiO_2. This behavior can be attributed to the so-called *Schottky barrier*. The *Schottky barrier* is formed when a *n*-type semiconductor and a metal with different work functions are in contact. Thus, the flow of electrons will preferably be from the material with the lowest work function to the one with the highest. As Ag^0 has a work function of 4.74 eV and TiO_2 of 4.6 eV [1], the preferential flow of electrons is from the semiconductor to the metal until the Fermi energy of both reaches equilibrium. This leads to the formation of a potential barrier that hinders the transfer of electrons from the semiconductor to the metal. Thus, the Schottky barrier acts as an electron trap, reducing

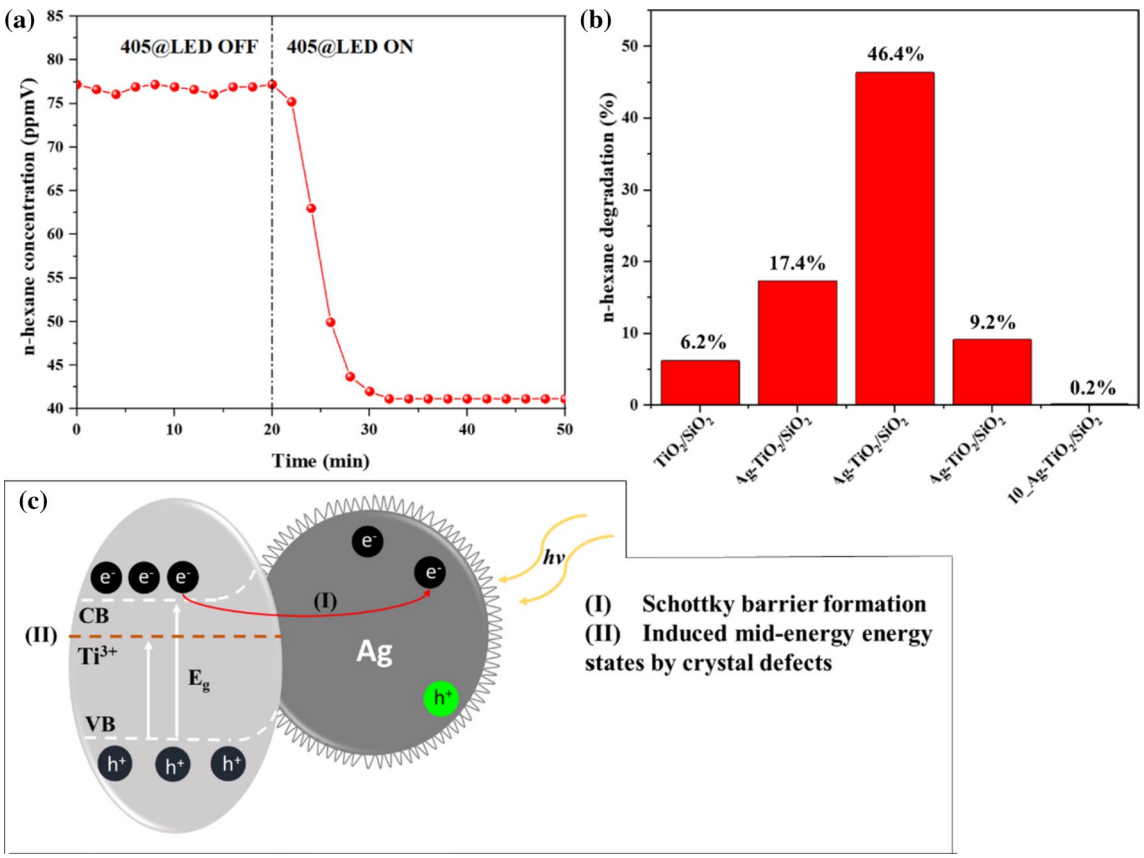

Figure 8 **a** Evolution of the concentration of *n*-hexane at the reactor outlet over time for 3_Ag-TiO_2/SiO_2; **b** % degradation of *n*-hexane obtained for the materials synthesized with 1, 3, 5, and 10% Ag; **c** photocatalytic mechanism proposed for TiO_2/SiO_2 materials modified with Ag.

charge recombination and consequently increasing the lifetime of photogenerated electrons by one to two orders of magnitude [30, 55]. Furthermore, it is suggested that the photocatalytic performance is also related to the formation of Ti^{3+} crystalline defects and oxygen vacancies on the anatase surface during the material synthesis, as evidenced by XPS and EPR analyses [33].

However, above the optimal value, Fig. 8b shows a drastic drop-in activity, with the 10_Ag_TiO_2SiO_2 material showing no appreciable degradation of *n*-hexane. Above an optimal metal content, silver started to have a detrimental effect on the activity of the material due to the following factors: (i) a high number of Ag^0 NPs should reduce the electron density, due the attraction of electrons by several particles simultaneously, resulting in a diffuse electric field that reduces charge separation, which is supported by EPR analyses; (ii) an excessive number of Ag NPs on the TiO_2 surface prevents light from reaching the semiconductor surface, consequently reducing the number of photogenerated charges, which impairs the photodegradation efficiency; and (iii) at higher Ag contents, the high surface free energy of silver promotes its segregation, thereby suppressing the formation of crystalline defects, as demonstrated by EPR analysis. As previously mentioned, this phenomenon prevents the occurrence of defects on the crystalline structure. In addition, as discussed from the SEM images (Fig. 3), at higher concentrations, silver tends to form clusters, becoming segregated from TiO_2, in addition to causing a reduction in the specific average particle size. This could also impair the photocatalytic activity of the material, as the agglomeration and segregation of silver nanoparticles reduce the specific surface area of contact between Ag NPs and TiO_2, hindering relevant phenomena for photocatalysis, such as the Schottky barrier, as well as altering the fluidization mechanics of the catalyst bed.

Figure 8c shows a schematic illustration of the Schottky Barrier formation and Ti^{3+} mechanism in Ag-loaded TiO_2. In addition to the mentioned mechanisms, the negligible photocatalytic performance exhibited by the 10_Ag_TiO_2/SiO_2 catalyst indicates that the photocatalytic activity under visible light is not driven by Ag NPs alone. As shown in the TEM and HRTEM images (Fig. 1b), for the 10_Ag_TiO_2/SiO_2 sample, the excess of Ag NPs caused the segregation of the nanoparticles, which were agglomerated and, in low content, on the TiO_2 surface. If Ag NPs were the only ones responsible for the photoactivity of the material, it would be expected that sample 10_Ag_TiO_2/SiO_2 would exhibit higher photoactivity. Therefore, its behavior suggests that the Ag NPs worked together with TiO_2/SiO_2, through Schottky barrier phenomenon and driving the formation of crystal defects (Ti^{3+} and oxygen vacancies) as previously discussed.

The photocatalytic oxidation mechanism of *n*-hexane can be triggered by the reactive species that occurring in the material. Firstly, according to the standard reduction potentials of $HO^{\bullet}/OH^{-}$ (1.9 eV vs. SHE) and $HO^{\bullet}/H_2O$ (2.72 eV vs. SHE) [34, 77], the holes in the valence band of TiO_2 can oxidize OH^{-} and H_2O induced by the humidity, generating hydroxyl radicals, since the valence band potential of the materials (Table 2) is higher than the standard potentials of the half-reactions. In addition, according to the standard reduction potential of $O_2/O_2^{\bullet-}$ (− 0.33 eV vs. SHE) [34, 77], the reduction of O_2 to superoxide radical anions is not allowed since the conduction band potential of the materials (Table 2) is higher than the standard reduction potential of the half-reaction $O_2 + e^{-} \rightarrow O_2^{\bullet-}$.

Conclusions

XPS and EPR analyses showed that Ag drove the formation of crystal defects on the surface of anatase grains during the reduction of AgO and Ag_2O to Ag metal in the calcination step. XRD results revealed that Ag loading induced the formation of brookite crystalline phase and crystal growth. Ag-loading of TiO_2/SiO_2 resulted in the narrowing of the band gap, due to the PRET mechanism, induced by the LSPR phenomenon, and Ti^{3+} defects on the anatase surface. The photodegradation of *n*-hexane in the continuous gas-phase photoreactor was efficient under visible light (> 400 nm), reaching 46.2% for the 3_Ag_TiO_2/SiO_2 catalyst, while the unloaded material (TiO_2/SiO_2) achieved 6.0% *n*-hexane degradation.

Together with the results of the characterization analyses, these findings highlight that the increase in photocatalytic activity is due to the Schottky barrier and the formation of crystal defects (Ti^{3+} and oxygen vacancies) on the surface of the anatase grains. Considering the application in a continuous gas-phase reactor, it is worth mentioning that we have developed a synthesis method that can be potentially applied to other photocatalytic materials. Subsequently, it was observed that increasing the silver

content up to 3% was beneficial for the photocatalytic activity, and above this, a marked decrease in *n*-hexane degradation under visible light was observed. Above an optimum Ag content, silver nanoparticles intensified charge recombination, decreased electron density, and possibly blocked irradiation of the TiO_2 surface.

Acknowledgement

This study was financed in part by the Coordenação de Aperfeiçoamento de Pessoal de Nível Superior – Brasil (CAPES) – Finance Code 001. The authors also express their gratitude to the National Council of Scientific and Technological Development (CNPq, Brazil, grants #311230/2020-2 and #140347/2020-8) and to the São Paulo Research Foundation (FAPESP, grant 2019/24158-9) for financial support. Moreover, this research used facilities of the Brazilian Nanotechnology National Laboratory (LNNano), part of the Brazilian Centre for Research in Energy and Materials (CNPEM), a private non-profit organization under the supervision of the Brazilian Ministry for Science, Technology, and Innovations (MCTI). The Naga Vishnu Vardhan Mogili and Ângela Albuquerque Teixeira Neto staff are acknowledged for the assistance during the experiments (TEM-FEG-20210327, XPS-20220414). Finally, the authors would like to thank Dr. Jose Geraldo Pacheco for their valuable contribution toward conducting photoluminescence spectroscopy analyses at Federal University of Pernambuco (UFPE).

Author contributions

CAG helped in conceptualization, methodology, validation, formal analysis, investigation, writing—original draft, and visualization. PHP was involved in methodology, validation, formal analysis, investigation, writing—original draft, and visualization. BR participated in formal analysis, investigation, writing–original draft, and visualization. ORJ helped in formal analysis, investigation, and visualization. DG was involved in investigation, visualization, and writing—review and editing. ACSCT participated in conceptualization, validation, resources, writing—original draft, writing—review and editing, supervision, and funding acquisition. All authors read and approved the final manuscript.

Funding

Coordenação de Aperfeiçoamento de Pessoal de Nível Superior—Brasil (CAPES—Coordination for the Improvement of Higher Education Personnel)–Finance Code 001, National Council of Scientific and Technological Development (CNPq, Brazil, grants #311230/2020–2 and #140347/2020–8), and the São Paulo Research Foundation (FAPESP, grant 2019/24158–9).

Data availability

All data generated or analyzed during this study are included in this published article and its supplementary information file.

Declarations

Conflict of interest The authors declare that they have no competing interests.

Ethical approval Not applicable.

Consent to participate Not applicable.

Consent for publication Not applicable.

Supplementary Information The online version contains supplementary material available at https://doi.org/10.1007/s10853-023-09285-7.

References

[1] Schneider J, Matsuoka M, Takeuchi M et al (2014) Understanding TiO_2 photocatalysis mechanisms and materials. Chem Rev 114:9919–9986. https://doi.org/10.1021/cr5001892

[2] Lim TH, Kim SD (2004) Trichloroethylene degradation by photocatalysis in annular flow and annulus fluidized bed photoreactors. Chemosphere 54:305–312. https://doi.org/10.1016/S0045-6535(03)00753-7

[3] Kamal MS, Razzak SA, Hossain MM (2016) Catalytic oxidation of volatile organic compounds (VOCs)-a review. Atmos Environ 140:117–134. https://doi.org/10.1016/j.atmosenv.2016.05.031

[4] Zhang X, Gao B, Creamer AE et al (2017) Adsorption of VOCs onto engineered carbon materials: a review. J Hazard Mater 338:102–123. https://doi.org/10.1016/j.jhazmat.2017.05.013

[5] Ozturk B, Yilmaz D (2006) Absorptive removal of volatile organic compounds from flue gas streams. Process Saf Environ Prot 84:391–398. https://doi.org/10.1205/psep05003

[6] Li Q, Li FT (2020) Recent advances in surface and interface design of photocatalysts for the degradation of volatile organic compounds. Adv Coll Interface Sci 284:102275. https://doi.org/10.1016/j.cis.2020.102275

[7] Huang Y, Ho SSH, Niu R et al (2016) Removal of indoor volatile organic compounds via photocatalytic oxidation: a short review and prospect. Molecules 21(1):56. https://doi.org/10.3390/molecules21010056

[8] Khan F, i, Ghoshal AKr, (2000) Removal of volatile organic compounds from polluted air. J Loss Prev Process Ind 13:527–545. https://doi.org/10.1016/S0950-4230(00)00007-3

[9] Mamaghani AH, Haghighat F, Lee C-S (2018) Gas phase adsorption of volatile organic compounds onto titanium dioxide photocatalysts. Chem Eng J 337:60–73. https://doi.org/10.1016/j.cej.2017.12.082

[10] Ojala S, Pitkäaho S, Laitinen T et al (2011) Catalysis in VOC abatement. Top Catal 54:1224–1256. https://doi.org/10.1007/s11244-011-9747-1

[11] Mansoubi H, Fatemi S, Mansourpour Z (2018) An efficient photo-catalytic VOC removal process by one-pot synthesized N-F/TiO_2 nanoparticles in fluidized-spouted bed reactor. Part Sci Technol 36:162–171. https://doi.org/10.1080/02726351.2016.1236048

[12] Mahdy AG, Emam AA, Mussa EA et al (2023) Synthesis and characterization of Li2$Mn_{0.8}Ni_{0.2}SiO_4$/Mn_3O_4 nanocomposite for photocatalytic degradation of reactive blue (RB5) dye. J Inorg Organomet Polym 33:1280–1297. https://doi.org/10.1007/s10904-023-02572-5

[13] Palharim PH, Caira'Amaro MCD, De Araújo Gusmão C et al (2022) Effect of temperature and time on the hydrothermal synthesis of WO_3-AgCl photocatalysts regarding photocatalytic activity. Chem Eng Res Des 188:935–953. https://doi.org/10.1016/j.cherd.2022.10.045

[14] Palharim PH, Diego L, dos Reis FB, Ramos B et al (2022) Effect of HCl and HNO_3 on the synthesis of pure and silver-based WO_3 for improved photocatalytic activity under sunlight. J Photochem Photobiol, A 422:113550. https://doi.org/10.1016/j.jphotochem.2021.113550

[15] Basseem M, Emam AA, Kamal FH et al (2023) Novel functionalized of ZnO with Sm^{3+}, La^{3+}, and Sr^{2+}/ZnO single and tri-doped nanomaterials for photocatalytic degradation: synthesis, DFT, kinetics. J Mater Sci 58:13346–13372. https://doi.org/10.1007/s10853-023-08829-1

[16] Basseem M, Emam AA, Kamal FH et al (2023) Photocatalytic activity of co-doped NPs based on ZnO as a new class of anti-microbial agents: Synthesis, characterization, kinetics, isotherm, and in silico molecular docking simulation. Appl Organomet Chem 37(10):e7238. https://doi.org/10.1002/aoc.7238

[17] Shayegan Z, Lee CS, Haghighat F (2018) TiO_2 photocatalyst for removal of volatile organic compounds in gas phase–a review. Chem Eng J 334:2408–2439. https://doi.org/10.1016/j.cej.2017.09.153

[18] Xu G, Zheng Z, Wu Y, Feng N (2009) Effect of silica on the microstructure and photocatalytic properties of titania. Ceram Int 35:1–5. https://doi.org/10.1016/j.ceramint.2007.09.008

[19] de Luna MDG, Laciste MT, Tolosa NC, Lu MC (2018) Effect of catalyst calcination temperature in the visible light photocatalytic oxidation of gaseous formaldehyde by multi-element doped titanium dioxide. Environ Sci Pollut Res 25:15216–15225. https://doi.org/10.1007/s11356-018-1720-0

[20] Zhang H, Jiang Y, Zhou B et al (2021) Preparation and photocatalytic performance of silver-modified and nitrogen-doped TiO_2 nanomaterials with oxygen vacancies. New J Chem 45:4694–4704. https://doi.org/10.1039/d0nj04755d

[21] Yguerabide J, Yguerabide EE (1998) Light-scattering submicroscopic particles as highly fluorescent analogs and their use as tracer labels in clinical and biological applications II. Exp Charact Anal Biochem 262:157–176. https://doi.org/10.1006/abio.1998.2760

[22] Fang M, Tan X, Liu Z et al (2021) Recent progress on metal-enhanced photocatalysis: a review on the mechanism. Research 2021:9794329. https://doi.org/10.34133/2021/9794329

[23] Dey D, Halder N, Misra KP et al (2020) Systematic study on the effect of Ag doping in shaping the magnetic properties of sol-gel derived TiO_2 nanoparticles. Ceram Int 46:27832–27848. https://doi.org/10.1016/j.ceramint.2020.07.282

[24] Einaga H (2006) Effect of silver deposition on tio for photocatalytic oxidation of benzene in the gas phase. React Kinet Catal Lett 88:357–362. https://doi.org/10.1007/s11144-006-0072-9

[25] Li X, Zou X, Qu Z et al (2011) Photocatalytic degradation of gaseous toluene over Ag-doping TiO_2 nanotube powder prepared by anodization coupled with impregnation method. Chemosphere 83:674–679. https://doi.org/10.1016/j.chemosphere.2011.02.043

[26] Liao G, Fang J, Li Q et al (2019) Ag-Based nanocomposites: Synthesis and applications in catalysis. Nanoscale 11:7062–7096. https://doi.org/10.1039/c9nr01408j

[27] Santos LM, Machado WA, França MD et al (2015) Structural characterization of Ag-doped TiO_2 with enhanced photocatalytic activity. RSC Adv 5:103752–103759. https://doi.org/10.1039/c5ra22647c

[28] Yaqoob AA, Umar K, Ibrahim MNM (2020) Silver nanoparticles: various methods of synthesis, size affecting factors and their potential applications–a review. Appl Nanoscie (Switzerland) 10:1369–1378. https://doi.org/10.1007/s13204-020-01318-w

[29] Zhao W, Zhang Z, Zhang J et al (2016) Synthesis of Ag/TiO_2/graphene and its photocatalytic properties under visible light. Mater Lett 171:182–186. https://doi.org/10.1016/j.matlet.2016.02.063

[30] Li Z, Wang S, Wu J, Zhou W (2022) Recent progress in defective TiO_2 photocatalysts for energy and environmental applications. Renew Sustain Energy Rev 156:111980. https://doi.org/10.1016/j.rser.2021.111980

[31] Na S, Seo S, Lee H (2020) Recent developments of advanced Ti^{3+}-self-doped TiO_2 for efficient visible-light-driven photocatalysis. Catalysts 10(6):679. https://doi.org/10.3390/catal10060679

[32] Xiu Z, Guo M, Zhao T et al (2020) Recent advances in Ti^{3+} self-doped nanostructured TiO2 visible light photocatalysts for environmental and energy applications. Chem Eng J 382:123011. https://doi.org/10.1016/j.cej.2019.123011

[33] Chao HE, Yun YU, Xingfang HU, Larbot A (2003) Effect of silver doping on the phase transformation and grain growth of sol-gel titania powder. J Eur Ceram Soc 23:1457–1464. https://doi.org/10.1016/S0955-2219(02)00356-4

[34] Gusmão CA, Palharim PH, Ramos B, Teixeira ACSC (2021) Enhancing the visible-light photoactivity of silica-supported TiO_2 for the photocatalytic treatment of pharmaceuticals in water. Environ Sci Pollut Res 29:42215–42230. https://doi.org/10.1007/s11356-021-16718-w

[35] Puddu V, Choi H, Dionysiou DD, Puma GL (2010) TiO_2 photocatalyst for indoor air remediation: Influence of crystallinity, crystal phase, and UV radiation intensity on trichloroethylene degradation. Appl Catal B 94:211–218. https://doi.org/10.1016/j.apcatb.2009.08.003

[36] Christoforidis KC, Figueroa SJA, Fernández-García M (2012) Iron-sulfur codoped TiO_2 anatase nano-materials: UV and sunlight activity for toluene degradation. Appl Catal B 117–118:310–316. https://doi.org/10.1016/j.apcatb.2012.01.029

[37] Laciste MT, de Luna MDG, Tolosa NC, Lu MC (2017) Degradation of gaseous formaldehyde via visible light photocatalysis using multi-element doped titania nanoparticles. Chemosphere 182:174–182. https://doi.org/10.1016/j.chemosphere.2017.05.022

[38] Araña J, Alonso AP, Rodríguez JMD et al (2009) FTIR study of photocatalytic degradation of 2-propanol in gas phase with different TiO_2 catalysts. Appl Catal B 89:204–213. https://doi.org/10.1016/j.apcatb.2008.11.027

[39] Almeida Diniz L, Matsumoto D, Silva Costa Teixeira AC (2021) Photocatalytic degradation of *n*-hexane in a circulating fluidized bed: an investigation based on the freeboard entrainment model. Catal Today 361:109–116. https://doi.org/10.1016/j.cattod.2020.01.043

[40] Bueno-Alejo CJ, Hueso JL, Mallada R et al (2019) High-radiance LED-driven fluidized bed photoreactor for the complete oxidation of *n*-hexane in air. Chem Eng J 358:1363–1370. https://doi.org/10.1016/j.cej.2018.09.223

[41] Geng Q, Guo Q, Yue X (2010) Adsorption and photocatalytic degradation kinetics of gaseous cyclohexane in an annular fluidized bed photocatalytic reactor. Ind Eng Chem Res 49:4644–4652. https://doi.org/10.1021/ie100114e

[42] Park JH, Seo YS, Kim HS, Kim IK (2011) Photodegradation of benzene, toluene, ethylbenzene and xylene by fluidized bed gaseous reactor with TiO_2/SiO_2 photocatalysts. Korean J Chem Eng 28:1693–1697. https://doi.org/10.1007/s11814-011-0021-9

[43] Liu C, Yang D, Jiao Y et al (2013) Biomimetic synthesis of TiO_2-SiO_2-Ag nanocomposites with enhanced visible-light photocatalytic activity. ACS Appl Mater Interfaces 5:3824–3832. https://doi.org/10.1021/am4004733

[44] Lee SK, Kim JS, Kim IK, Lee JK (2006) Photodegradation of a volatile organic compound by fluidized bed reactor with TiO_2/SiO_2 and metal-TiO_2/SiO_2. In: Rhee H-K, Nam I-S, Park JM (eds) Studies in surface science and catalysis. Elsevier, pp 581–584

[45] Chen Y, Wang K, Lou L (2004) Photodegradation of dye pollutants on silica gel supported TiO_2 particles under visible light irradiation. J Photochem Photobiol, A 163:281–287. https://doi.org/10.1016/j.jphotochem.2003.12.012

[46] Liao J, Yang F, Wang C-Z, Lin S (2018) The crystal facet-dependent electrochemical performance of TiO_2 nanocrystals for heavy metal detection: theoretical prediction and experimental proof. Sens Actuators, B Chem 271:195–202. https://doi.org/10.1016/j.snb.2018.05.067

[47] Wu X-P, Yang M-Y, Zhou Z-J, et al (2023) Chapter 16 - Photocatalysis. In: García-Iriepa C, Marazzi M (eds) Theoretical and Computational Photochemistry. Elsevier, pp 387–415

[48] Di Paola A, Cufalo G, Addamo M et al (2008) Photocatalytic activity of nanocrystalline TiO_2 (brookite, rutile and brookite-based) powders prepared by thermohydrolysis of $TiCl_4$ in aqueous chloride solutions. Colloids Surf, A

317:366–376. https://doi.org/10.1016/j.colsurfa.2007.11.005

[49] Mahshid S, Askari M, Ghamsari MS (2007) Synthesis of TiO_2 nanoparticles by hydrolysis and peptization of titanium isopropoxide solution. J Mater Process Technol 189:296–300. https://doi.org/10.1016/j.jmatprotec.2007.01.040

[50] Carp O, Huisman CL, Reller A (2004) Photoinduced reactivity of titanium dioxide. Prog Solid State Chem 32:33–177. https://doi.org/10.1016/j.progsolidstchem.2004.08.001

[51] Tian Z, Du S, Cheng X et al (2022) The Role of oxygen vacancy in anatase to rutile transformation of TiO_2. Cryst Growth Des 22:6852–6856. https://doi.org/10.1021/acs.cgd.2c01062

[52] Elahifard M, Sadrian MR, Mirzanejad A et al (2020) Dispersion of defects in TiO_2 semiconductor: oxygen vacancies in the bulk and surface of rutile and anatase. Catalysts 10(4):397. https://doi.org/10.3390/catal10040397

[53] Bensouici F, Souier T, Dakhel AA et al (2015) Synthesis, characterization and photocatalytic behavior of Ag doped TiO_2 thin film. Superlattices Microstruct 85:255–265. https://doi.org/10.1016/j.spmi.2015.05.028

[54] Ly NH, Vasseghian Y, Joo S-W (2023) Plasmonic photocatalysts for enhanced solar hydrogen production: a comprehensive review. Fuel 344:128087. https://doi.org/10.1016/j.fuel.2023.128087

[55] Khan MR, Chuan TW, Yousuf A et al (2015) Schottky barrier and surface plasmonic resonance phenomena towards the photocatalytic reaction: study of their mechanisms to enhance photocatalytic activity. Catal Sci Technol 5:2522–2531. https://doi.org/10.1039/c4cy01545b

[56] Wang L, Sun Y, Xu B (2007) Comparison study on the microstructure of nanocrystalline TiO_2 in different Ti-Si binary oxides. J Mater Sci Technol 23:604–610

[57] Boukis N, Claussen N, Ebert K et al (1997) Corrosion screening tests of high-performance ceramics in supercritical water containing oxygen and hydrochloric acid. J Eur Ceram Soc 17:71–76. https://doi.org/10.1016/S0955-2219(96)00072-6

[58] Braconnier B, Páez CA, Lambert S et al (2009) Ag- and SiO_2-doped porous TiO_2 with enhanced thermal stability. Microporous Mesoporous Mater 122:247–254. https://doi.org/10.1016/j.micromeso.2009.03.007

[59] Neaţu Ş, Pârvulescu VI, Epure G et al (2009) M/TiO_2/SiO_2 (M=Fe, Mn, and V) catalysts in photo-decomposition of sulfur mustard. Appl Catal B 91:546–553. https://doi.org/10.1016/j.apcatb.2009.06.026

[60] Suligoj A, Stangar UL, Ristic A et al (2016) TiO_2–SiO_2 films from organic-free colloidal TiO_2 anatase nanoparticles as photocatalyst for removal of volatile organic compounds from indoor air. Appl Catal B 184:119–131. https://doi.org/10.1016/j.apcatb.2015.11.007

[61] Liu X, Zhang Y, Matsushima S et al (2020) Photocatalytic oxidation process for treatment of gas phase benzene using Ti^{3+} self-doped TiO_2 microsphere with sea urchin-like structure. Chem Eng J 402:126220. https://doi.org/10.1016/j.cej.2020.126220

[62] Kumar R, El-Shishtawy RM, Barakat MA (2016) Synthesis and characterization of Ag-Ag_2O/TiO_2@polypyrrole heterojunction for enhanced photocatalytic degradation of methylene blue. Catalysts 6(6):76. https://doi.org/10.3390/catal6060076

[63] Palomino RM, Hamlyn R, Liu Z et al (2017) Interfaces in heterogeneous catalytic reactions: ambient pressure XPS as a tool to unravel surface chemistry. J Electron Spectrosc Relat Phenom 221:28–43. https://doi.org/10.1016/j.elspec.2017.04.006

[64] Ghattavi S, Nezamzadeh-Ejhieh A (2019) A brief study on the boosted photocatalytic activity of AgI/WO_3/ZnO in the degradation of methylene blue under visible light irradiation. Desalin Water Treat 166:92–104. https://doi.org/10.5004/dwt.2019.24638

[65] Nezamzadeh-Ejhieh A, Bahrami M (2015) Investigation of the photocatalytic activity of supported ZnO–TiO_2 on clinoptilolite nano-particles towards photodegradation of wastewater-contained phenol. Desalin Water Treat 55:1096–1104. https://doi.org/10.1080/19443994.2014.922443

[66] Lan D, Wu H, Puleo F, Liotta LF (2019) Bulk and surface characterization techniques of TiO_2 and TiO_2-doped oxides. In: Marcì G, Palmisano L (eds) Heterogeneous Photocatalysis. Elsevier, Amsterdam, pp 57–86. https://doi.org/10.1016/B978-0-444-64015-4.00003-1

[67] Liang Y, Huang G, Xin X et al (2022) Black titanium dioxide nanomaterials for photocatalytic removal of pollutants: a review. J Mater Sci Technol 112:239–262. https://doi.org/10.1016/j.jmst.2021.09.057

[68] Nair RV, Gummaluri VS, Matham MV, Vijayan C (2022) A review on optical bandgap engineering in TiO_2 nanostructures via doping and intrinsic vacancy modulation towards visible light applications. J Phys D: Appl Phys 55(31):313003. https://doi.org/10.1088/1361-6463/ac6135

[69] Wang L, Wang X, Yin J et al (2016) Silica induced oxygen vacancies in supported mixed-phase TiO_2 for photocatalytic degradation of phenol under visible light irradiation. Catal Commun 87:98–101. https://doi.org/10.1016/j.catcom.2016.09.011

[70] Vasilaki E, Vernardou D, Kenanakis G et al (2017) TiO_2/WO_3 photoactive bilayers in the UV–Vis light

region. Appl Phys A 123:231. https://doi.org/10.1007/s00339-017-0837-1

[71] Yao N, Huang J, Fu K et al (2016) Reduced interfacial recombination in dye-sensitized solar cells assisted with NiO:Eu^{3+}, T^{b3}+ coated TiO_2 film. Sci Rep 6:31123. https://doi.org/10.1038/srep31123

[72] Lim SP, Pandikumar A, Lim HN et al (2015) Boosting photovoltaic performance of dye-sensitized solar cells using silver nanoparticle-decorated N, S-Co-Doped-TiO_2 photoanode. Sci Rep 5:11922. https://doi.org/10.1038/srep11922

[73] Tang B, Chen H, Peng H, Wang Z, Huang W (2018) Graphene modified TiO_2 composite photocatalysts: Mechanism, Progress and Perspective. Nanomater 8(2):105. https://doi.org/10.3390/nano8020105

[74] Patra KK, Bharad PA, Jain V, Gopinath CS (2019) Direct solar-to-hydrogen generation by quasi-artificial leaf approach: possibly scalable and economical device. J Mater Chem A 7:3179–3189. https://doi.org/10.1039/C8TA11307F

[75] Mehrabadi Z, Faghihian H (2019) Clinoptilolite modified TiO_2 for simultaneouos elimination of two herbicides; 2,4-D and MCPA by UV and sunlight-assisted photocatalytic degradation. Mater Res Bull 119:110569. https://doi.org/10.1016/j.materresbull.2019.110569

[76] Le THT, Bui TT, Van Bui H et al (2021) TiO_2 inverse opals modified by ag nanoparticles: a synergic effect of enhanced visible-light absorption and efficient charge separation for visible-light photocatalysis. Catalysts 11(7):761. https://doi.org/10.3390/catal11070761

[77] de Araújo GC, Diniz LA, Ramos B, Câmara AG, Pacheco JG, Teixeira AC (2022) Optimization of TiO_2/SiO_2 photocatalysts in a LED-irradiated gas-solid photoreactor for air treatment. Chem Eng Res Des 185:223–238. https://doi.org/10.1016/j.cherd.2022.07.001